



HAL
open science

Stereoscopic Measurements of Coronal Doppler Velocities

O. Podladchikova, L. Harra, K. Barczynski, C. H. Mandrini, F. Auchere, D. Berghmans, E. Buchlin, L. Dolla, M. Mierla, S. Parenti, et al.

► **To cite this version:**

O. Podladchikova, L. Harra, K. Barczynski, C. H. Mandrini, F. Auchere, et al.. Stereoscopic Measurements of Coronal Doppler Velocities. *Astronomy & Astrophysics - A&A*, 2021, 655, pp.A57. 10.1051/0004-6361/202140457 . hal-03415315

HAL Id: hal-03415315









<https://hal.science/hal-03415315v1>

Submitted on 21 Apr 2023

HAL is a multi-disciplinary open access archive for the deposit and dissemination of scientific research documents, whether they are published or not. The documents may come from teaching and research institutions in France or abroad, or from public or private research centers.

L'archive ouverte pluridisciplinaire **HAL**, est destinée au dépôt et à la diffusion de documents scientifiques de niveau recherche, publiés ou non, émanant des établissements d'enseignement et de recherche français ou étrangers, des laboratoires publics ou privés.

Stereoscopic measurements of coronal Doppler velocities[★]

O. Podladchikova¹, L. Harra^{1,2}, K. Barczynski^{1,2}, C. H. Mandrini³, F. Auchère⁴, D. Berghmans⁵,
É. Buchlin⁴, L. Dolla⁵, M. Mierla^{5,6}, S. Parenti⁴, and L. Rodriguez⁵

¹ Physikalisch-Meteorologisches Observatorium Davos, World Radiation Center, 7260 Davos Dorf, Switzerland
e-mail: elena.podladchikova@pmodwrc.ch

² ETH-Zürich, Wolfgang-Pauli-Str. 27, 8093 Zürich, Switzerland

³ Instituto de Astronomía y Física del Espacio, IAFE, UBA-CONICET, Ciudad Universitaria, CC. 67, 1428 Buenos Aires, Argentina

⁴ Université Paris-Saclay, CNRS, Institut d'Astrophysique Spatiale, 91405 Orsay, France

⁵ Solar-Terrestrial Centre of Excellence – SIDC, Royal Observatory of Belgium, Ringlaan-3-Av. Circulaire, 1180 Brussels, Belgium

⁶ Institute of Geodynamics of the Romanian Academy, 19-21 Jean-Louis Calderon, 020032 Bucharest, Romania

Received 30 January 2021 / Accepted 26 July 2021

ABSTRACT

Context. The Solar Orbiter mission, with an orbit outside the Sun-Earth line and leaving the ecliptic plane, opens up opportunities for the combined analysis of measurements obtained by solar imagers and spectrometers. For the first time different space spectrometers will be located at wide angles to each other, allowing three-dimensional (3D) spectroscopy of the solar atmosphere.

Aims. The aim of this work is to prepare a methodology to facilitate the reconstruction of 3D vector velocities from two stereoscopic line of sight (LOS) Doppler velocity measurements using the Spectral Imaging of the Coronal Environment (SPICE) on board the Solar Orbiter and the near-Earth spectrometers, while widely separated in space.

Methods. We developed the methodology using the libraries designed earlier for the STEREO mission, but applied to spectroscopic data from the Hinode mission and the Solar Dynamics Observatory. We used well-known methods of static and dynamic solar rotation stereoscopy and the methods of extreme ultraviolet (EUV) stereoscopic triangulation for optically thin coronal EUV plasma emissions. We developed new algorithms using analytical geometry in space to determine the 3D velocity in coronal loops.

Results. We demonstrate our approach with the reconstruction of 3D velocity vectors in plasma flows along ‘open’ and ‘closed’ magnetic loops. This technique will be applied to an actual situation of two spacecraft at different separations with spectrometers on board during the Solar Orbiter nominal phase: SPICE versus the Interface Region Imaging Spectrograph (IRIS) and Hinode imaging spectrometer. We summarise how these observations can be coordinated.

Key words. techniques: imaging spectroscopy – Sun: corona – Sun: UV radiation – Sun: heliosphere – instrumentation: high angular resolution – instrumentation: spectrographs

1. Introduction

The Solar Orbiter (SO) space mission (Müller et al. 2020), launched in February 2020, provides both remote sensing and in situ measurements of the solar atmosphere and heliosphere. The main goal of this mission is to understand how the heliosphere is formed and sustained. The trajectory of SO takes it out of the Earth’s orbit and into an orbit around the Sun, reaching to within 0.28 AU of the orbit of Mercury. A spacecraft whose orbit is away from the Sun-Earth line opens up huge possibilities for the representation of the three-dimensional (3D) imaging and spectroscopic data together with near-Earth imaging and spectroscopy. For the first time spectrometers will be located at different angles from each other, allowing 3D spectroscopy of the solar atmosphere.

The presence of persistent high-temperature, high-speed upflows from the edges of active regions (Harra et al. 2008) is a key discovery from Hinode (Culhane et al. 2007). Measurements from the extreme ultraviolet (EUV) Imaging Spectrometer (EIS) indicate that the upflows reach velocities of 50 km s^{-1} with spectral line asymmetries approaching 100 km s^{-1} and more (see e.g. Dolla & Zhukov 2011). It has been suggested that

these upflows may lie on open magnetic field lines that connect to the heliosphere and may be a significant source of the low-speed solar wind (Harra et al. 2008; Brooks & Warren 2011; Mandrini et al. 2014, and references therein). All of the active regions observed by Hinode/EIS show upflows. Different explanations have been given for the physical mechanism of the upflows, including waves, reconnection in the corona (Baker et al. 2009; Mandrini et al. 2015), and reconnection in the chromosphere (De Pontieu et al. 2007) driving energy upwards. The blue-shifts in these regions are ubiquitous, and indicate the presence of upflows. Various studies have used modelling to determine whether the upflows that are seen at the edges of the active regions become plasma outflowing into the solar wind (e.g. Boutry et al. 2012; Edwards et al. 2016).

Attempts have been made to understand how these flows vary with the location on the disc. Limb-to-limb studies of an active region were carried out by Démoulin et al. (2013) and Baker et al. (2017). The highest plasma velocities in the three spectral lines that they explored have similar magnitudes, and their magnitudes increase with temperature. The authors concluded that their results are compatible with the active-region upflows originating from reconnection between active-region loops and neighbouring loops. However, having two spectroscopic views of an active region will enhance our understanding of flows.

* Movies associated to Fig. 1 are available at <https://www.aanda.org>

The first work on solar stereoscopy was carried out by assuming temporal stability of the features under study and allowing the Sun to rotate in order to obtain more than one viewpoint (e.g. [Berton & Sakurai 1985](#); [Koutchmy & Molodenskii 1992](#); [Aschwanden & Bastian 1994](#); [Aschwanden et al. 1995, 1999](#); [Feng et al. 2007a](#)). This approach is used also now (see e.g. [Nisticò et al. 2013](#)). The review by [Aschwanden \(2011\)](#) presents in detail the methods of static and dynamic solar rotation stereoscopy for coronal loops observed in optically thin coronal plasma EUV emissions.

Two simultaneous viewpoints of the Sun were provided by the Solar Terrestrial Relations Observatory (STEREO, [Kaiser et al. 2008](#)). The two STEREO spacecraft orbit the Sun with increasing separation angles, providing stereoscopic images of the Sun's atmosphere. The stereoscopic images obtained by the two nearly identical EUV broad-band imagers of the Sun Earth Connection Coronal and Heliospheric (SECCHI) suite ([Howard et al. 2008](#); [Wuelser et al. 2004](#); [Eyles et al. 2009](#)) on board STEREO helped us to understand the 3D geometry of a rich variety of optically thin solar structures ([Liewer et al. 2009](#); [Patsourakos et al. 2009](#); [Aschwanden 2009a](#); [West et al. 2011](#); [Delannée et al. 2014](#); [Podladchikova et al. 2019](#); [Mierla et al. 2008, 2009, 2010](#); [Temmer et al. 2009](#); [Feng et al. 2009](#); [de Patoul et al. 2013](#)). Methods of stereoscopic triangulation using a stereoscopic pair of EUV or white light coronal images have been developed. A great deal of progress has been made to improve magnetic field models based on stereoscopic information, and to reduce the discrepancy between theoretical magnetic field models and observed stereoscopically triangulated loop 3D coordinates ([Aschwanden 2011](#)).

Several studies have been carried out in parallel to calculate the true location of coronal structures in 3D space ([Pizzo & Biesscker 2004](#); [Inhester 2006](#); [Feng et al. 2007b](#); [Aschwanden et al. 2008](#); [Howard & Tappin 2008](#)). These studies are based on the direct geometric triangulation using a series of line-of-sight (LOS) measurements taken from different spacecraft views towards the apparent edges of the structures. The true 3D coordinates of the structures are calculated from the intersections of these LOSs. The theoretical background for solar stereoscopy based on the direct triangulation of solar structures is given by [Inhester \(2006\)](#). The direct triangulation technique can be applied after prior identification and matching of the targeted structures in two images (see the review by [Wiegmann et al. 2009](#)). An alternative method of magnetic stereoscopy is proposed by [Wiegmann & Neukirch \(2002\)](#). The success of magnetic stereoscopy depends on the quality of theoretical magnetic field models. A critical assessment of non-linear force-free field (NLFFF) models has identified a substantial mismatch between theoretical magnetic field models extrapolated from photospheric magnetograms and stereoscopically triangulated loops, of the order of a 3D misalignment angle of $\alpha_{\text{mis}} \approx 20^\circ$ to 40° ([De Rosa et al. 2009](#); [Sandman et al. 2009](#); [Aschwanden 2011](#)). [Rodríguez et al. \(2009\)](#) highlighted that every pixel in an image is a result of the LOS integration of the emission of the optically thin coronal plasma. This problem of LOS integration persists in the analysis of the EUV data, further complicating the matching of points between the two images.

The triangulation method has been applied to detailed 3D reconstructions of coronal loops in active regions obtained from a stereoscopic pair of images ([Inhester 2006](#); [Aschwanden et al. 2008, 2012a, 2015](#); [Aschwanden & Wülser 2011](#); [Nisticò et al. 2013](#); [Chifu et al. 2017](#)). An example of such work ([Rodríguez et al. 2009](#)) reveals that loops that appear to be co-spatial in 171 Å and 195 Å images in fact have different

heights and occupy different volumes. These results are key to understanding coronal heating.

In this paper we develop a 3D EUV spectroscopy methodology for active regions that is used to build velocity vectors from a pair of EUV images and from Doppler shift maps taken from different perspectives. We do this using the STEREO triangulation technique of EUV images of active regions and we develop novel methods of analytical geometry in space to determine 3D velocities in coronal loops. An advantage of having two different views of an active region is that we can determine the projection angles of the loops, and hence direction of plasma flows along them. We used Hinode/EIS data acquired at different times in order to replicate the situation of two spacecraft with spectrometers on board, and we chose an active region that did not show significant changes in time (Sect. 2). In addition, we describe the methods with which we can reconstruct the velocity vectors; they will be released as a suite of 3D spectroscopy algorithms called the DOppler VElocities Stereoscopically (DOVES) software package, for velocity vector reconstruction. We describe the spatio-temporal co-alignment between EUV broad-band and spectroscopic images (Sect. 3), the reconstruction of the 3D geometry of coronal loops (Sect. 4), and deprojection algorithms of the measured LOS Doppler shifts into velocity vectors of plasma flows onto straight and curved coronal loop structures (Sect. 5). We also describe the magnetic field modelling of the active region to investigate the possibility of using it to derive the 3D loop geometry (Sect. 5.2.4).

A description of the instruments that could be used for 3D spectroscopy is given in Sect. 6. We provide recommendations on the optimum possible spacecraft configuration and spatial resolution of the instruments for 3D spectroscopy within the framework of the Solar Orbiter mission. The proposed 3D spectroscopy method is of particular interest to understanding how the corona is heated and how the solar wind is formed.

2. Data preparation for 3D spectroscopy

2.1. Instrumentation

Initial data for 3D velocity reconstruction includes a stereoscopic pair of EUV images, and simultaneous Doppler shift measurements from two angularly separated spectrometers. To simulate the stereo view we obtain usable simultaneous datasets with SPICE, and we use solar rotation to produce two different viewpoints, as was done for the STEREO software preparation. These viewpoints are imitated now by imaging data obtained by the Atmospheric Imaging Assembly (AIA) on board the Solar Dynamic Observatory (SDO, [Pesnell et al. 2012](#)) and spectroscopic data from Hinode/EIS. By applying direct triangulation methods to SDO/AIA intensity images, we restore the 3D coordinates of the observed structures. Then the triangulation of the Doppler shifts observed by Hinode/EIS allows us to restore the vector velocities in these structures.

Hinode is a Japanese mission launched in 2006 by the Institute of Space and Astronautical Science (ISAS) of the Japan Aerospace Exploration Agency (JAXA) in collaboration with the National Astronomical Observatory of Japan ([Kosugi et al. 2007](#)). Hinode/EIS has two wavelength bands, 170–211 Å and 246–292 Å, that include spectral lines formed over a wide range of temperatures, from chromospheric to flare temperatures. Hinode/EIS has an effective spatial resolution of about 3–4 arcsec. The high spectral resolution (0.06 Å) allows the determination of Doppler velocity maps with an accuracy of 3 km s^{-1} . The Hinode/EIS campaign used in this work has a slit

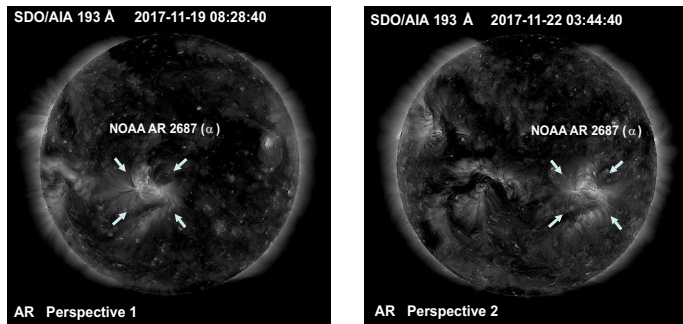


Fig. 1. Whole Sun images obtained with SDO/AIA at 193 Å on 19 November 2019 (position 1, *left*) and 22 November 2017 (position 2, *right*). The active region (indicated by arrows) has a simple magnetic configuration (α according to the Zurich classification). These two views correspond to a separation of 37° between position 1 and position 2, allowing the use of stereoscopy for the 3D reconstruction of the active region. The active region dynamic evolution is illustrated with four animations: 193 Å from 19 to 22 November (*Movie 1*), stabilized 193 Å from 19 to 22 November (*Movie 2*), 2D SDO/HMI photospheric magnetic field with overlaid 193 Å (*Movie 3*), 171 Å (*Movie 4*). The animations demonstrate that some of the observed simple shape loops can be traced throughout the entire animation.

size of 1 arcsec, a field of view (FOV) of $467 \text{ arcsec} \times 511 \text{ arcsec}$ and a raster duration of 67 min.

The SDO/AIA, built by Lockheed Martin Solar and Astrophysics Laboratory, provides continuous broad-band full-disc images from the chromosphere to the solar corona in seven EUV wavelengths covering the temperature range $2 \times 10^4 - 2 \times 10^7 \text{ K}$, with a cadence of 12 s and a spatial resolution of 1.2 arcsec (corresponding to two pixels). The SDO is in a circular geosynchronous orbit at an altitude of 35 800 km.

Active region NOAA AR 2678 was observed simultaneously by SDO/AIA and Hinode EIS on 19 and 22 November 2017. The separation of the two observing positions due to solar rotation is 37° , which is within the angular range $9^\circ - 120^\circ$ in which stereoscopic vision and 3D spectroscopy becomes applicable. We discuss this aspect in Sect. 3.

2.2. Observations of NOAA AR 2678

On each viewpoint, three simultaneous images were obtained: (1) Fe XII intensity from SDO/AIA, (2) Fe XII intensity from Hinode EIS, and (3) Fe XII Doppler velocity map. The SDO/AIA images are used to establish the 3D coordinates of coronal points and the Hinode EIS images for velocity vector construction in 3D space. Figure 1 shows whole Sun images obtained with SDO/AIA at 193 Å. Because the active region evolves slowly, its apparent morphological changes are due to the different viewing angles.

3. Spatio-temporal data co-alignment for 3D spectroscopy

3.1. Hinode/EIS data

We used the `eis_prep.pro` routine in Solar Software to calibrate the Hinode/EIS data. The dark current and cosmic rays were removed, and the hot pixels were corrected. The intensity digital number (DN) values were calibrated to the spectral radiance in units of $\text{erg} (\text{cm}^2 \text{sr} \text{Å})^{-1}$. We focused on the strongest emission line observed by Hinode EIS, Fe XII at 195.12 Å with for-

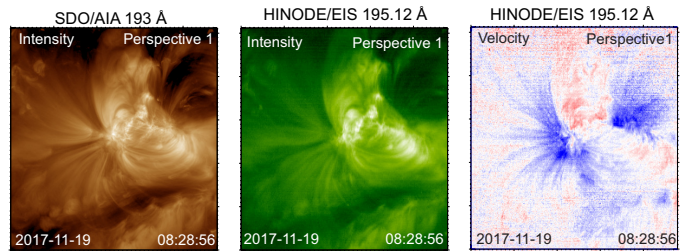


Fig. 2. Hinode/EIS intensity (*middle*) and Doppler velocity (*right*) raster maps with corrected pointing information, and the spatio-temporally corresponding artificial SDO/AIA raster map (*left*) obtained by the instruments in position 1.

mation temperatures $\log T = 6.1$. For each spectrum we fitted a single-Gaussian function rather than a double-Gaussian function with the `eis_auto_fit` routine and obtained the line peak intensity, Doppler velocity, and line width using `eis_get_fitdata.pro`.

3.2. SDO/AIA data processing

We chose the following conditions for the SDO/AIA 193 Å data; the observation time corresponds to that of the whole Hinode/EIS raster scan. The FOV is slightly larger than the region observed by Hinode/EIS and it is tracked with solar rotation at the Carrington rate. Images were transformed to a grid with a resolution of 0.6 arcsec per pixel. The pre-processed data were aligned with the solar north and divided by the exposure time. The strongly saturated frames were removed. We selected SDO/AIA 193 Å images with more than 2 s of exposure time to obtain suitable images for long-lived coronal structure analysis. We processed the images with an image stacking technique to increase photon-to-noise statistics and then with a wavelet high-pass filter to enhance coronal structures (Stenborg et al. 2008).

3.3. Hinode/EIS and SDO/AIA data co-alignment

Dynamic structures on the solar surface evolve over a significantly shorter time than the duration of the Hinode/EIS raster observation of 67 min. We created a pseudo SDO/AIA raster analogous to the Hinode/EIS raster to compensate for possible dynamic changes. To this end, we extracted the SDO/AIA data closest in time to each position of the Hinode/EIS slit. These data were merged into a single SDO/AIA map (hereafter referred to as the artificial SDO/AIA raster map), corresponding to the Hinode/EIS raster map using the cross-correlation method described here. The offset between the artificial SDO/AIA raster map and the Hinode/EIS raster map was applied, together with a pointing correction. Based on the new Hinode/EIS pointing details, the new artificial SDO/AIA raster map was created and aligned to the new Hinode/EIS map. In our analysis, we set the expected accuracy to half the size of the Hinode/EIS pixel.

Figure 2 shows the Hinode/EIS intensity and Doppler velocity raster maps and the corresponding artificial SDO/AIA raster map. A similar procedure was presented in Barczynski et al. (2018) to co-align SDO/AIA and the Interface Region Imaging Spectrometer (IRIS) raster data. Here 3D point triangulation is performed with SDO/AIA data, and each 3D point is assigned to a pair of Doppler shifts via spatio-temporal SDO/AIA–Hinode/EIS co-alignment.

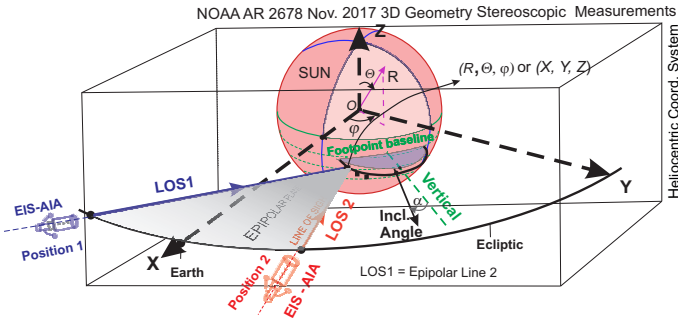


Fig. 3. Stereoscopic observation of NOAA AR 2678 with two spacecraft. The positions of the two spacecraft and any point in the solar corona to be triangulated define a plane called the epipolar plane (see e.g. Inhester 2006). Because LOS1 and LOS2 must lie in the same epipolar plane, their intersection in this plane is unambiguously defined by the 3D point. For convenience, the 3D coordinates of the points are reconstructed in HEEQ heliocentric coordinates (the x -axis is directed towards the Earth). Calculation of the 3D point coordinates is the first step in the velocity vector construction.

4. 3D triangulation of NOAA AR 2678

4.1. Triangulation through epipolar geometry

The 3D coordinates are calculated as (Earth-based) Stonyhurst heliographic longitude and latitude, along with the radial distance in solar radii. Then the coordinates are converted into the Heliocentric Earth Equatorial (HEEQ) coordinates for a Cartesian representation of the data. A two-dimensional (2D) solar image taken by a spacecraft is usually identified by the (i, j) coordinates in the image coordinate system or by the latitude and longitude in the heliographic (or helioprojective Cartesian) coordinate system, when (i, j) are projected on the solar surface (Thompson 2006). The multi-point heliospheric observation in the corona requires a complete 3D heliocentric coordinate system, as explained in Sect. 4.1.1. Figure 3 shows the HEEQ coordinate system with the origin in the centre of the Sun and the object position in the heliosphere described by the Cartesian coordinates X, Y, Z . The Stonyhurst coordinate system describes the 3D position of a feature with the spherical coordinates R, Θ, φ .

As Fig. 3 shows, two observing spacecraft positions together with a targeted point in the solar corona define a plane called the epipolar plane. All targeted points have planes in common that contain the two spacecraft positions. Given that every epipolar plane is seen head-on from both spacecraft, it is reduced to a line in the respective image projections. This line is called an epipolar line.

Any targeted corona point found to be situated on a certain epipolar line in one image must lie on the same epipolar line in the other image. The epipolar lines therefore provide a natural coordinate system for stereoscopic reconstructions. Consequently, finding a correspondence between pixels in the images taken by two EUV imagers separated in space is reduced to establishing a correspondence between pixels along the same epipolar lines in the two images.

Once the correspondence between the pixels is found, the 3D reconstruction is performed by calculating the LOSs that belong to the respective pixels in the image and back-tracking them into 3D space. Because the LOSs must lie in the same epipolar plane, their intersection in this plane is defined unambiguously. This procedure is often called ‘tie-pointing’ (see e.g. Inhester 2006; Mierla et al. 2009; Liewer et al. 2009; Aschwanden 2011). The

geometrical reconstruction errors are related to both the separation angle γ between the two spacecraft and the spatial resolution d_s of an image (Inhester 2006; Aschwanden et al. 2015); see Sect. 6.3 for more information on reconstruction errors in the context of the Solar Orbiter mission.

4.1.1. 3D triangulation software

In this study, we use the HEEQ system. The origin of the HEEQ system is the intersection of the solar equator with the central meridian as seen from Earth, and the solar feature location is given either in Cartesian coordinates X, Y, Z (HEEQ coordinates) or in spherical coordinates (Stonyhurst heliographic coordinates: latitude Θ , longitude φ and heliospheric radius R) (Thompson 2006) (see Fig. 3). The locations of the features were processed with the World Coordinate System routine `scc_measure.pro` of the Solar Software (Thompson 2006). The structures were traced in stereoscopic pairs of images using projections along the epipolar lines. The routine uses a combination of the information in the header, such as the pixel-to-degree conversion, and the Spacecraft Planet Instrument C-matrix Events orientation (SPICE) database of orbital kernels by calling the routine `convert_sunspice_coord.pro`, which is based on SPICE orbital ephemeris kernels containing the spacecraft location and pointing information. The coordinate system of each spacecraft image plane can be related to a heliocentric coordinate system, and stereoscopic analysis is performed. The output of `scc_measure.pro` is given in the Stonyhurst heliographic coordinates.

4.1.2. 3D triangulation of AR 2678 points

Direct measurement of the 3D coordinates of a point located high in the solar corona is not possible. However, if the two LOSs traced back from the LOS projections on the 2D image intersect higher in the corona at the observed point, then the 3D coordinates of the point can be evaluated. The procedure is performed as follows:

- Point selection on a 2D plane of sky (Image 1); see Fig. 4a.
- Transition to 3D coordinates.
- LOS drawing from satellite 1 to the observed point (LOS 1 or epipolar lines in stereoscopy). The LOSs are not visible on the 2D Image 1 (Fig. 4a), because they are projected to one point.
- Image 2 (Fig. 4b) shows the same area in the solar corona from Perspective 2. LOS1 is visible in Image 2 (Fig. 4b) thanks to observation from a different point.
- The intercept of LOS 1 with coronal loops, the structure of the observation, determines the projection of the 3D point on Image 2 (crosses in Fig. 4b). Thus, the problem converges as long as we deal with two LOS projections of the same point in 3D space.

To check the obtained coordinates the procedure can be then performed in reverse order (Figs. 4c and d). In Fig. 4d we start from the obtained points on Image 2 and describe how we arrive at the initially selected points on Image 1 (Fig. 4c) using the LOS projection technique. We repeat the procedure for points 1, 2, and 3 located on the same loop (and for points 4, 5 and 6, 7) selected on the SDO/AIA images, and express their true spatial position in a 3D heliocentric coordinate system.

4.2. NOAA AR 2678 3D loop triangulation

Here we study the loops, shown in Fig. 4 as straight, curved, or semicircular, which is typical for loops that are inclined towards

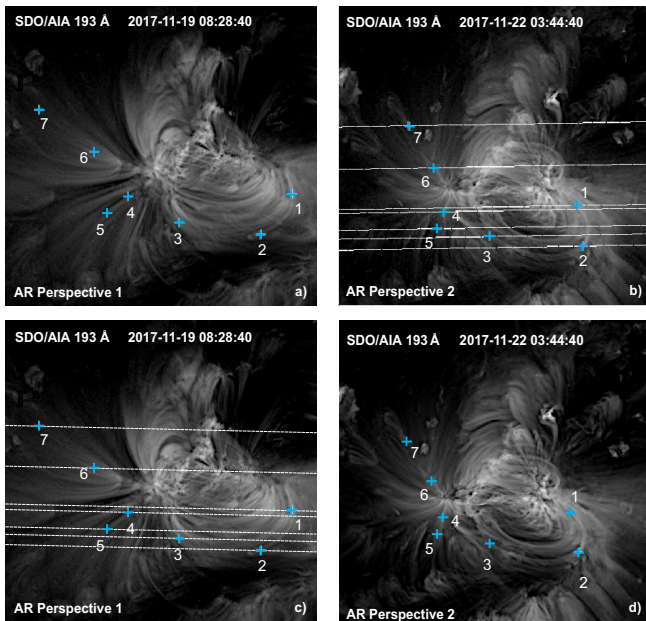


Fig. 4. (a) Points 1 to 7 on Image 1 selected for triangulation. (b) Points 1 to 7 on Image 2 are found on the corresponding epipolar lines (dashed lines) at the intersection with the observed structures. Points 1, 2, and 3 belong to closed loops (i.e. where both of their bases can be identified in AIA EUV images); whereas points 4, 5, 6, and 7 belong to open loops (i.e. where only one of their bases can be identified AIA EUV images). To validate the tie-pointing procedure the reverse process was performed, first starting from the obtained points in Image 2 (panel d) and then selecting their stereoscopic pairs on the corresponding epipolar lines in Image 1 (panel c), obtaining the same points.

the surface near the centre of the disc (Reale 2010). Aschwanden (2011) presents the technique of semi-circular loop point positions and loop plane inclination definitions. The plane in the strict geometric sense has zero thickness; nevertheless, the terms ‘loop plane’ and ‘loop plane inclination’ are the established and widely used terms in the analysis of the parameters of coronal loops (see e.g. the section ‘Stereoscopic Fitting of Circular Loop Geometry’ in Aschwanden 2009b, or Nisticò et al. 2013; Aschwanden & Wülser 2011), even though the real loops are thick (Klimchuk et al. 1992).

From the 3D triangulation we obtain several points on the same loop. We model the loop as a circle, as explained in Rodríguez et al. (2009) and Aschwanden (2011), defining the curvature radius, and we use three loop points triangulated as described above to fit the loop with the model. The loop can be defined in 3D space by a set of three points with coordinates (X, Y, Z) in the HEEQ coordinate system, and the two sets of 2D coordinates of the solar images $(i_{\text{Los1}}, j_{\text{Los1}})$ and $(i_{\text{Los2}}, j_{\text{Los2}})$; however, it is possible to use more points to fit the circle. We save the projected coordinates of the 3D points $(i_{\text{Los}}, j_{\text{Los}})$ on the images obtained from the two perspectives for the subsequent operations with Doppler velocity measurements. More details on loop parametrisation are given in Aschwanden et al. (2015), Aschwanden (2011), and Nisticò et al. (2013).

When working with optically thin objects in the solar corona, the most critical task is to ensure that two LOSs truly intersect on the object under study in 3D EUV images of the corona. Figure 5 shows the coronal loop under study, presented in the 3D HEEQ coordinate system and reconstructed from points 1, 2, and 3. Blue lines outside the loop show tangents to the loop plotted at the observed points.

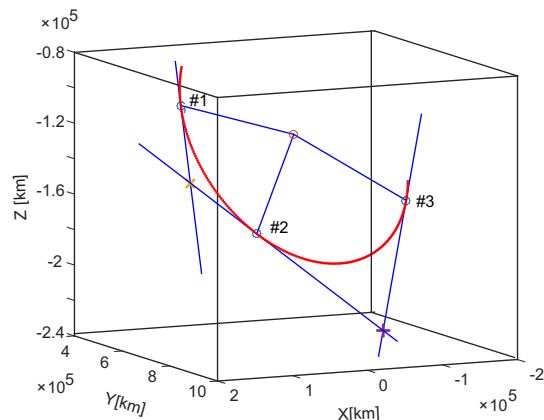


Fig. 5. Semi-circular curved coronal loop under study observed stereoscopically in NOAA AR 2678 in November 2017. The loop is shown in the HEEQ coordinate system. The blue lines outside the loop show tangents to the loop plotted at the selected points.

Table 1 summarises the results of the 3D reconstructed points in the Stonyhurst coordinate system from the perspective on Earth, and from the perspectives of Position 1 and Position 2. The first entry in the table lists the results for points selected on a closed loop within the active region core, where the dominant Doppler velocity indicates a downflow, and the bottom part of the table shows results for points on open loops at the edges of the active region, where the Doppler velocities show blue-shifted plasma (upflow). We note that we use the term ‘closed loops’ for those for which we can identify their two bases in the AIA EUV images and ‘open loops’ for those for which we can identify only one of their bases in the AIA EUV images.

5. 3D spectroscopy methodology

5.1. Vector velocity measurements

We developed a sequence of algorithms designed to perform triangulation of Doppler shift maps of the solar corona recorded from different perspectives, with the ultimate goal of enabling reconstruction of the vector velocity field.

Solar-rotation stereoscopy was used to reconstruct the 3D coordinates of the highly elevated points in the solar corona. The same loops were identified in two 2D EUV images in order to calculate the true loop location in 3D corona coordinates. We used the coronal loops of NOAA AR 2678 projected on the plane of the sky observed by SDO/AIA from two different viewing angles (Figs. 6a and b). The region was stable in time and did not show any flaring activity, as demonstrated by Animation 1. The crosses in the images show the different locations of the elevated coronal points when they are projected through the LOS onto 2D images. The SDO/AIA images and Hinode/EIS intensity images were co-aligned as described in Sect. 3 (Figs. 6c and d). As long as the Hinode/EIS intensity and velocity maps are co-aligned, the crosses on the intensity maps can be directly translated onto the velocity maps. Thus, the crosses on the two Hinode EIS velocity maps indicate two LOS velocities measured in the considered elevated coronal points (Figs. 6e and f).

5.2. Velocity vectors for NOAA AR 2678 coronal loops

In this section we describe how to obtain a velocity vector at a point situated high above the photospheric level, using two LOS

Table 1. NOAA AR 2678 3D loop triangulation results.

	Earth (Lat./Long.)	Position 1 (Lat./Long.)	Position 2 (Lat./Long.)	Height above photosphere	Inclination α degrees
<i>Closed loop</i>					
Point 1	-10.7°/-3.04°	-13.2°/-3.13°	-12.7°/35.16°	16.0 Mm	
Point 2	-12.9°/5.2°	-16.6°/-5.9°	-16.2°/36.40°	76.1 Mm	15.5°
Point 3	-12.9°/-12.2°	-15.6°/-12.9°	-15.3°/26.2°	29.6 Mm	
<i>Open loop</i>					
Point 4	-10.9°/-16.5°	-13.4°/-17.24°	-13.2°/21.3°	22.3 Mm	
Point 5	-11.7°/-17.5°	-14.8°/-19.2°	-14.6°/21.4°	55.1 Mm	54.1°
<i>Open loop</i>					
Point 6	-6.9°/-18.5°	-9.6°/-19.9°	-9.3°/20.02°	48.8 Mm	
Point 7	-3.2°/-21.7°	-5.90°/-24.7°	-5.7°/17.4°	89.1 Mm	55.5°

Notes. Latitude, longitude, and height above the photosphere of the seven selected points in Fig. 4. Column 1 indicates the point number. Columns 2, 3, and 4 show the latitude and longitude from Earth, Position 1 viewpoint, and Position 2 viewpoint, respectively. Column 5 lists the height of the points above the photosphere, and Col. 6 shows the inclination angles α between either the open or closed coronal loop plane and the vertical to the solar surface. See text for the meaning of closed and open loops.

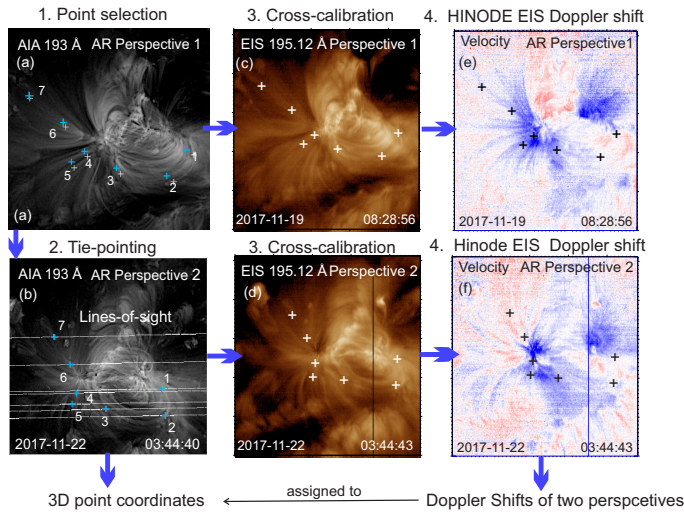


Fig. 6. Stereoscopic view of NOAA AR 2678, recorded from different perspectives in November 2017. (a) and (b) show the elevated 3D points projected on the 2D SDO/AIA intensity maps through the LOS technique. LOS1 from Perspective 1 (panel a) is projected downwards in Image 2 (panel b). Crosses denote the projection of the elevated coronal points in 2D images. Cross-calibration has been applied for the SDO/AIA and Hinode/EIS images (panels c and d). The Hinode/EIS intensity and Doppler velocity maps match, as long as they are obtained by the same spectrometer at the same time. The LOS projections of the elevated points on the 2D Doppler velocity maps (panels e and f) provide two LOS velocity values attached to their reference point in 3D space. The majority of the reconstructed points are associated with upflows (blue) and only two points are associated with downflows (red).

Doppler measurements obtained by spectrometers distributed in the heliosphere. Previously, we restored the true 3D coordinates of points in the high corona and the coordinates of their projections onto each of the 2D Doppler maps.

5.2.1. Deprojection rules of two LOS velocity components in the epipolar plane

Observing two LOS Doppler velocities at any identifiable point in the corona enables us, first of all, to find the velocity vector in the epipolar plane formed in the 3D heliosphere by the

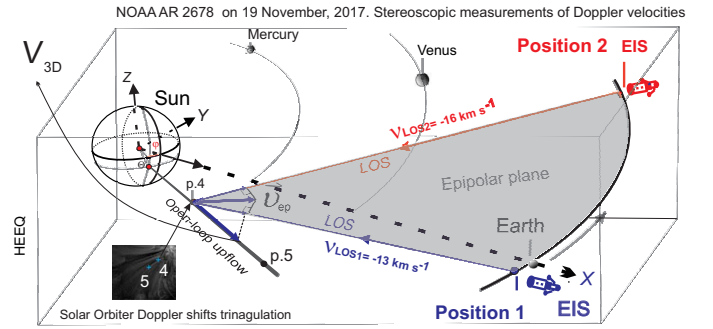


Fig. 7. Stereoscopic observation of NOAA AR 2678 on 19 November 2017, shown in the 3D HEEQ coordinate system. The X-axis is directed towards the Earth and the Z-axis is aligned with the solar rotation axis passing through the solar north. The two observing satellites are separated from each other by 37°. The blue-shifts at point 4 are measured along their respective LOSs and are represented by the vector magnitudes $v_{\text{LOS}1}$ and $v_{\text{LOS}2}$. The velocity vector v_{ep} , measured in the epipolar plane, is calculated from $v_{\text{LOS}1}$ and $v_{\text{LOS}2}$ following the geometry depicted in the figure. In this case the true velocity vector of point 4 is directed along the coronal loop, showing the plasma flow confined by the magnetic field, and it is calculated directly from the deprojection of V_{3D} on the coronal loop. If the plasma flow is perpendicular to the epipolar plane, its velocity cannot be measured, i.e. V_{3D} cannot be derived when it makes an angle of 90° degrees with the epipolar plane.

position of the two satellites and the observation point. The grey plane in Fig. 7 shows the epipolar plane defined by the observed point 4 on the open coronal loop and the location of the two satellites. The two Doppler blue-shifted velocities measured at point 4 along the LOSs situated between the observed point and the observing satellites represent the 1D vectors $v_{\text{LOS}1}$ and $v_{\text{LOS}2}$. Figure 8 shows two LOS Doppler velocities measured at points 4, 5, 6, and 7. Here, $v_{\text{LOS}1}$ and $v_{\text{LOS}2}$ are different velocities measured along the LOSs. The velocity vector v_{ep} is the projection of the 3D velocity in the epipolar plane, and can be reconstructed by calculating the intersection point of the two perpendiculars deprojected from $v_{\text{LOS}1}$ and $v_{\text{LOS}2}$ in the epipolar plane. The velocity vector v_{ep} , defined in the epipolar plane, is an especially useful estimate when we cannot identify any structure to which this point belongs. In this case v_{ep} can be an indicator of the plasma flow behaviour.

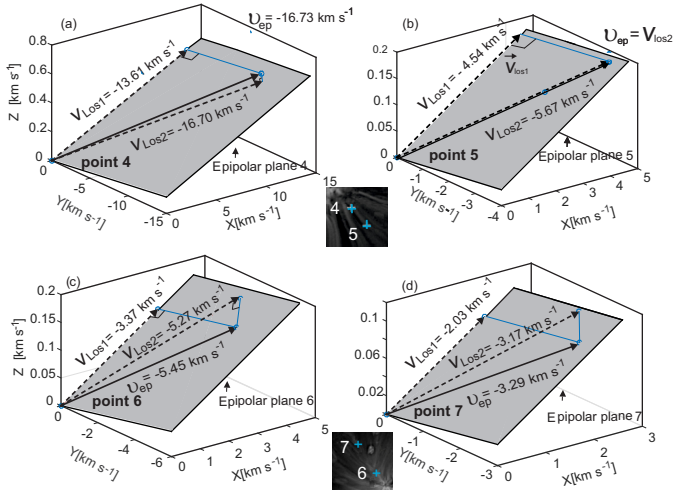


Fig. 8. Two LOS velocity components $v_{\text{LOS}1}$ and $v_{\text{LOS}2}$ (dashed arrows), measured by each spectrometer at points 4, 5, 6, and 7 in the corona and the reconstructed v_{ep} (solid arrows) in the epipolar plane (grey). The epipolar plane is defined by the locations of the two spacecraft and the point in the solar corona to be triangulated. v_{ep} represents the projection of $V_{3\text{D}}$ on the epipolar plane. When projected on LOS1 and LOS2, v_{ep} represents the velocities $v_{\text{LOS}1}$ and $v_{\text{LOS}2}$ measured by each spectrometer.

5.2.2. Plasma outflows along open loops

In this subsection we demonstrate the technique of velocity vector reconstruction in the open coronal loops using the pre-calculated geometry in 3D space. If the pair of points (4, 5) or (6, 7) belongs to the open coronal loop approximated as a straight line between two points, we can restore the velocity vector magnitude of the plasma flow by the direct deprojection of v_{ep} on the loop by using the formula

$$V_{3\text{D}} = \frac{v_{\text{ep}}}{\cos(\beta)}, \quad (1)$$

where β is the angle between the v_{ep} velocity and the coronal loop (Fig. 9). If $\beta = 90^\circ$, the deprojection cannot be made. Correspondingly, small β angles lead to higher accuracy of the $V_{3\text{D}}$ deprojection.

We reconstructed the velocity vector $V_{3\text{D}}$ for the points in the open-loop outflows using deprojections: $v_{\text{ep}} \rightarrow V_{3\text{D}}$. Figure 9 shows the locations of the coronal loop in 3D corona coordinates and the epipolar planes crossing loops at the points under observation, where two LOS Doppler velocities are measured and v_{ep} is obtained (blue arrows in the planes). After the measurement of the β angle between v_{ep} (blue arrows) and the loop in 3D space, we obtain $V_{3\text{D}}$ (black arrows along the loops) using Eq. (1). In all cases the resulting vector velocities $V_{3\text{D}}$ are directed outwards. The numerical values of the velocity vectors are given in Table 2. The small variation in the angle β between the LOS Doppler velocities (same spacecraft position) and the open loop when measured from points on the same loop reflects the location change of the observation point.

5.2.3. Plasma outflows in closed loops

In this subsection we demonstrate a technique for determining the velocity vector for flows following curved paths traceable in the solar corona. When measuring the LOS Doppler velocities with two spectrometers at points belonging to a closed, semi-

circular, or simply curved coronal structure, $V_{3\text{D}}$ can be determined again using Eq. (1). However, in this case the deprojection should be performed on the tangent to the coronal-loop direction, as long as the velocity vector is oriented in this direction. Figure 10 (left panel) shows the deprojected velocity v_{ep} from the two measured LOS Doppler velocities $v_{\text{LOS}1}$, $v_{\text{LOS}2}$. Figure 10 (right panel) shows $V_{3\text{D}}$ at points 1, 2, and 3. Detailed information on the LOS Doppler velocity magnitudes and their angles with the tangents are listed in Table 3.

Thus, the velocities deprojected from two LOS Doppler velocities measured at points of a closed coronal loop provide true intrinsic information of the plasma flow behaviour in the loop. In this case the deprojection is not carried out on the structure, as described in the previous subsection, but in the direction of the tangent to the loop reconstructed at the observed point. This technique can be applied to any curved structure in the solar atmosphere, provided that we can define its 3D geometry using, for instance, epipolar geometry stereoscopy or magnetic modelling of the loops.

5.2.4. Comparison of deduced inclinations and linear force-free field extrapolation of NOAA AR 2678

Magnetic field modelling has been used extensively to interpret the morphology of coronal magnetic loops (Chifu et al. 2015). An example by Harra et al. (2008) illustrates how using the angles from magnetic field modelling enables a more accurate determination of the upflowing plasma at the edge of an active region.

We compute the coronal magnetic field topology of NOAA AR 2678 during its disc transit on 11 November 2017 at 08:28 UT and 22 November 2017 at 03:44 UT. The LOS magnetic field is extrapolated to the corona using a linear force-free field (LFFF) configuration where $\mathbf{J} \times \mathbf{B} = 0$ and $\nabla \times \mathbf{B} = \alpha_M \mathbf{B}$, with α_M constant (Mandrini et al. 1996; Démoulin et al. 1997).

Figure 11 (left panel), shows the LFFF model results for 19 November 2017. Similar results are obtained on 22 November 2017 (right panel). Both panels show the modelled global coronal structure for which we have used the magnetograms closest in time to each EIS image as boundary condition. The panels are constructed superposing field lines computed using different values of α_M , which have been selected to better match the shape of the observed loops in AIA 193 Å. To do this comparison, the model is first transformed from the local frame to the observed frame, as discussed in Mandrini et al. (2015) (see the transformation equations in the appendix of Démoulin et al. 1997). This allows a direct comparison of our computed coronal field configuration to AIA EUV loops. Furthermore, in order to determine the best matching α_M values we have followed the procedure discussed by Green (2002).

Figure 12 shows the definition of the loop inclination angles δ_{EUV} computed for EUV SDO/AIA loops using triangulation methods, which are compared with those δ_M derived from our LFFF extrapolation. The inclination angles δ_M derived from the model are computed as discussed in Démoulin et al. (2013); they are the angles between the line tangential to the loop at the coronal points studied here and the vertical to the solar surface as shown in Fig. 12.

The LFFF and stereoscopic methods both obtained rather close ranges of inclination angles to the vertical: $[20^\circ, 30^\circ]$ at point 1 and $[35^\circ, 45^\circ]$ at point 3 on the closed loop. For open loops the inclination δ_{EUV} and δ_M to the vertical at point 6 and point 7 (where the field lines are quite simple) are in the same range $[10^\circ, 30^\circ]$. At point 4 and point 5 the inclination angles

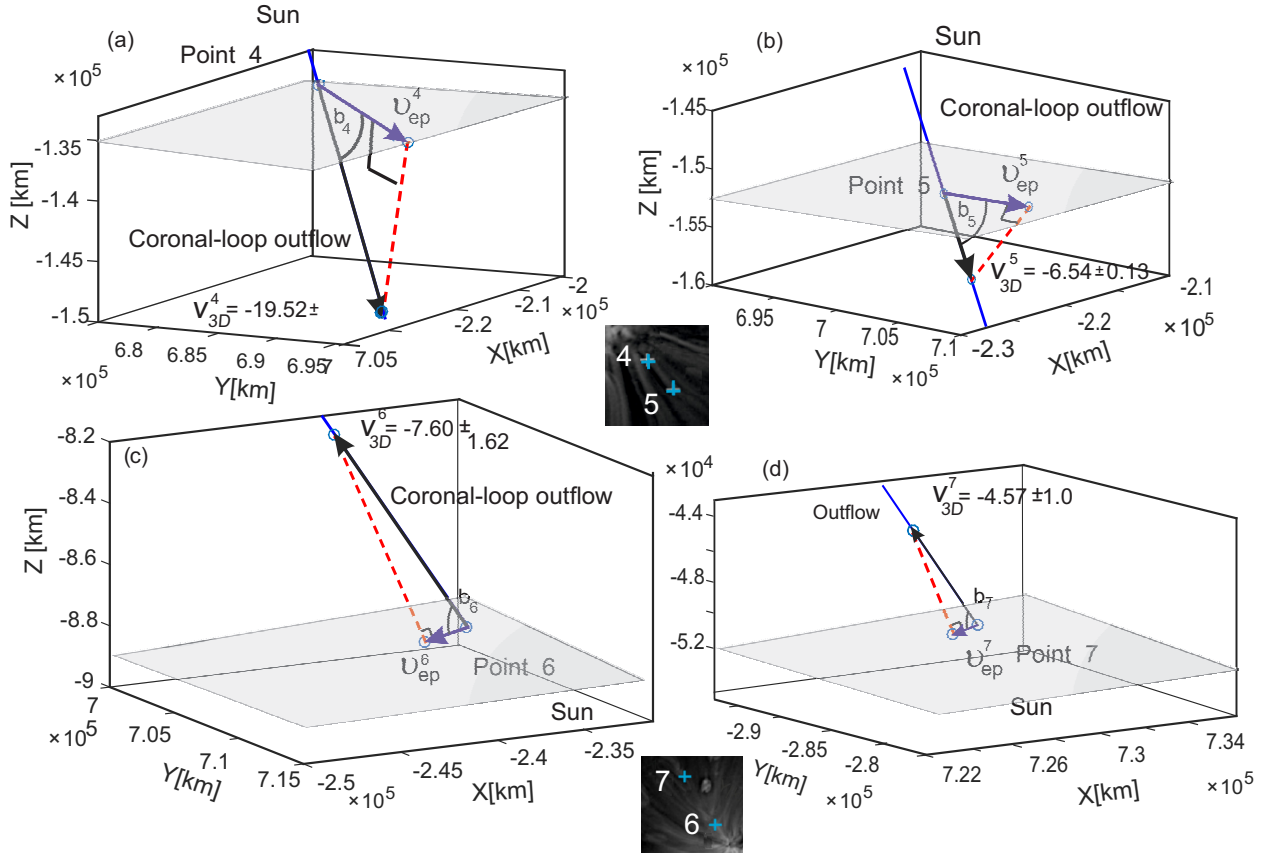


Fig. 9. Open loops traced in 3D solar coronal coordinates at points 4, 5 (panels a and b) and 6, 7 (panels c and d). The grey planes represent epipolar planes crossing the loops at the points under observation. The epipolar planes are formed in the heliosphere by the two spacecraft locations and each of the points 4, 5, 6, and 7; v_{ep} is reconstructed in the plane as shown in Fig. 8. The V_{3D} velocity vectors are reconstructed using the measured angle β and v_{ep} according to Eq. (1). The magnitudes of the vectors are shown in Table 2.

estimated by the two methods are in the range $[15^\circ, 25^\circ]$. Since the projection of an observed coronal loop has a certain thickness, a computed set of infinitely thin field lines can match the visible shape of a loop; this is the origin of the range of values for the inclination δ_M coming from the magnetic field model.

In general, we do not observe discrepancies between the field lines computed from the LFFF model and stereoscopic reconstruction, although photospheric footpoints are difficult to identify in EUV images, and from the magnetic model we trace the full line starting at the photospheric level. The latter demonstrates the future opportunity of pairing stereoscopic loop reconstruction using Solar Orbiter data with magnetic field modelling, which is expected to significantly improve the accuracy of stereoscopic vector velocity measurements (see e.g. Aschwanden et al. 2015).

6. 3D Spectroscopy by two distributed imaging spectrometers

We developed an approach using a pair of space-born spectrometers that provide stereoscopic views of Doppler shift maps in the solar corona. Measurement of the velocity vector in the corona can be achieved with one extraterrestrial remote spectrometer (SO/SPICE) and with the orbital spectrometer Hinode/EIS or IRIS. Dual spectrometers allow measurement of the 2D velocity vector in any identifiable coronal point, and eventually reconstruction of 3D velocity vectors, using the morphology of the coronal structures. In this section we describe how we derive the optimal spacecraft configurations for 3D spectroscopy with SO.

Table 2. Plasma flow velocities reconstructed in NOAA AR open loop 3D points.

	v_{LOS1} (km s^{-1})	v_{LOS2} (km s^{-1})	v_{ep} (km s^{-1})	β (degrees)	V_{3D} (km s^{-1})
<i>Open loop</i>					
Point 4	-13.61 km s^{-1}	-16.71 km s^{-1}	-16.73 km s^{-1}	28.86°	-19.11 km s^{-1}
Point 5	-4.54 km s^{-1}	-5.67 km s^{-1}	-5.67 km s^{-1}	28.54°	-6.45 km s^{-1}
<i>Open loop</i>					
Point 6	-3.37 km s^{-1}	-5.27 km s^{-1}	-5.45 km s^{-1}	36.29°	-6.76 km s^{-1}
Point 7	-2.03 km s^{-1}	-3.17 km s^{-1}	-3.29 km s^{-1}	36.32°	-4.07 km s^{-1}

Notes. Numerical values of the fully reconstructed velocity vectors V_{3D} , which characterise outflows along open loops shown by black arrows in Fig. 9. β is the angle between the velocity vector v_{ep} measured in the epipolar plane and the loop. V_{3D} can be reconstructed by deprojecting v_{ep} onto the coronal loop. The calculations were carried out for each of the points 4, 5, 6, and 7, which lie on open loops. The minus sign is implied to indicate outflows.

The spectral and spatial resolution of spectrometers influences directly the velocity vector measurement accuracy.

6.1. The SPICE, Hinode/EIS, and IRIS spectrometers

High-resolution spectroscopy of optically thin plasma allows measurements of plasma parameters such as temperatures, densities, chemical abundances, and Doppler and non-thermal motions (Phillips et al. 2008; Del Zanna & Mason 2018).

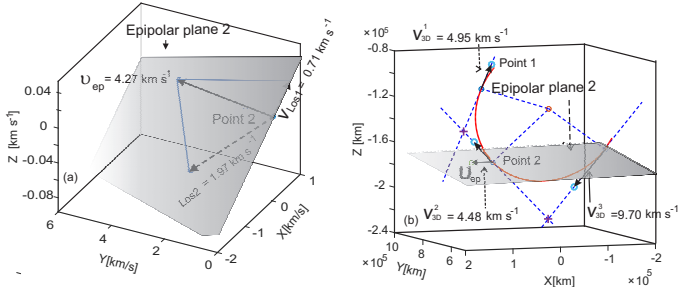


Fig. 10. Plasma flow velocity vectors in the 3D closed coronal loop under investigation. The location of the loop points in the high corona and the 3D geometry of the loop were determined using the LOS projection technique. *Panel a:* velocity vector v_{ep} , deprojected from the two Doppler LOS velocities measured by the two spectrometers at point 2. The epipolar plane (grey) is the plane containing the two satellites and the observation point. The vectors V_{3D} were constructed by the deprojection of v_{ep} on the tangent to the loop direction (*panel b*). The absolute values of the vectors are shown in Table 3.

Table 3. Plasma flow velocities reconstructed in NOAA AR closed loop 3D points.

	v_{LOS1} (km s^{-1})	v_{LOS2} (km s^{-1})	v_{ep} (km s^{-1})	β (degrees)	V_{3D} (km s^{-1})
<i>Closed loop</i>					
Point 1	2.38 km s^{-1}	-0.68 km s^{-1}	4.91 km s^{-1}	7.51°	4.95 km s^{-1}
Point 2	0.71 km s^{-1}	-1.97 km s^{-1}	4.27 km s^{-1}	17.98°	4.48 km s^{-1}
Point 3	-7.35 km s^{-1}	-9.4 km s^{-1}	-9.41 km s^{-1}	14.11°	-9.70 km s^{-1}

Notes. Velocity vectors characterising the flows in the investigated closed loops observed in NOAA AR2678 in November 2017. V_{3D} , shown in Fig. 10, is reconstructed at points 1, 2, and 3 on the loop. The velocity vectors V_{3D} are found by deprojection from v_{ep} on the tangent to the coronal loop directions. The minus sign indicates outflows.

In the science phase of the Solar Orbiter mission, there will be opportunities to carry out 3D spectroscopy in the chromosphere, transition region, and corona for the first time by combining data from Hinode/EIS (Culhane et al. 2007), IRIS (De Pontieu et al. 2014a), and SO/SPICE (Anderson et al. 2020). The Hinode/EIS wavelength ranges are 1170–210 Å and 250–290 Å, and its angular resolution is 2 arcsec. There are four slit and slot positions: 1 arcsec slit, 2 arcsec slit, 40 arcsec slot, and 266 arcsec slot. The temporal resolution is a few seconds in dynamic events, 10 s in active regions, and around 1 min in coronal holes. The maximum FOV is 360 arcsec \times 512 arcsec.

The SO/SPICE instrument is also a high-resolution imaging spectrometer operating at EUV/UV wavelengths. Its design is focused on studies that combine remote sensing and in situ instruments on board Solar Orbiter. The wavelength range is 704–790 Å and 973–1049 Å and the accuracy of the line shifts is 5 km s^{-1} . Table 4 shows the different emission lines used by SPICE, their wavelengths, temperature of formation, and their closest equivalents for Hinode/EIS. In most cases the emission lines for the two instruments do not represent the same ion, but the formation temperature is similar. Some caution must be used for lines that are optically thick, such as He II, when comparing them.

IRIS is an imaging spectrometer with a slit-jaw imaging system that probes the chromosphere. It explores the solar chromospheric dynamics to determine how the energy flows through the chromosphere and the transition region. The spacecraft has a polar sun-synchronous orbit. IRIS has a spatial resolution of

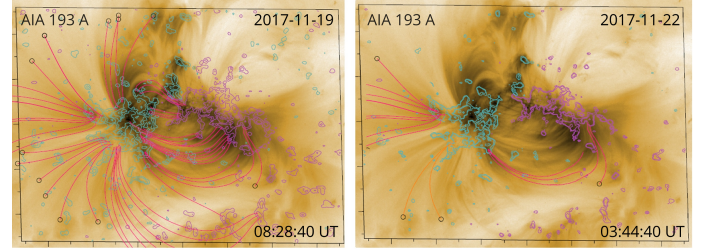


Fig. 11. LFFF extrapolation for NOAA AR2678 overlaid on an SDO/AIA intensity map. *Left panel:* LFFF model results at 08:28 UT on 19 November 2017. *Right panel:* LFFF model extrapolation at 03:44 UT on 22 November 2017.

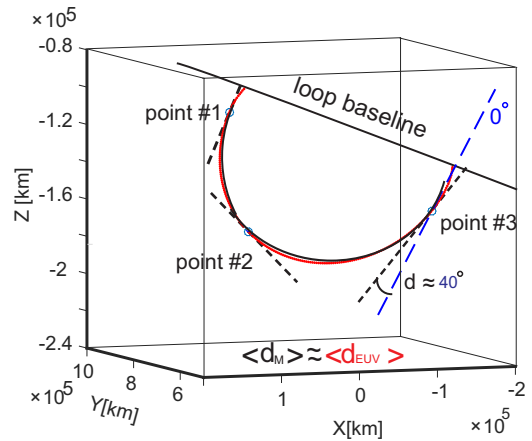


Fig. 12. Closed coronal loop of NOAA AR2678 traced in 3D corona coordinates by stereoscopic (red) and LFFF (black) methods. We computed here the inclination δ_{EUV} between the vertical to the solar surface (blue) and the tangential line at the studied points for SDO/AIA loops using stereoscopic methods and we found a close similarity with the δ_M computed using the LFFF extrapolations.

0.33–0.4 arcsec, a temporal resolution of 2 s, and a velocity resolution of 1 km s^{-1} over an FOV of up to 175 arcsec \times 175 arcsec (De Pontieu et al. 2007, 2014b).

IRIS and Hinode/EIS frequently carry out simultaneous observations, pointing at the same target. This mode of collaboration will be of great interest alongside the different FOVs of Solar Orbiter. The IRIS wavelength range covers the chromosphere, and the Hinode/EIS wavelength range covers the corona. The SPICE wavelength range provides measurements of the chromosphere, transition region, and corona. Combining the three spectrometers will provide the first 3D solar spectroscopy. Table 5 shows a comparison of the SPICE and IRIS wavelengths.

6.2. SPICE observing with the Extreme Ultraviolet Imager and SDO/AIA

For 3D geometry reconstruction, we used SDO/AIA intensity images and their coupling with Doppler velocity maps to perform operations with vector velocities. In this context Solar Orbiter Doppler maps can be combined with the intensity images of the Extreme Ultraviolet Imager (EUI) on board the same satellite. In both cases the match between Doppler maps and intensity images provides all the data necessary to compute velocity vectors.

The EUI (Rochus et al. 2019) on board Solar Orbiter observes the solar atmosphere from the top of the chromosphere

Table 4. SPICE emission lines, wavelength, temperature of formation (T), and the closest equivalents in Hinode/EIS.

SPICE	Wavelength (Å)	log T	EIS	Wavelength (Å)	log T
C III	977.03	4.5	He II	256.7	4.7
O V	760.43	5.4	O V	192.9	5.4
Ne VIII	770.92	5.8	Mg VII	278.39, 280.75	5.8
			Si VII	275.35	5.8
			Fe VIII	185.21, 194.66	5.8
Mg IX	706.02	6.0	Fe X	184.5, 257.2	6.0
Fe X	1028.04	6.0			
Mg XI	997.44	6.2	Fe XIII	196.54, 202.04, 203.83	6.2
Si XII	520.67	6.3	Fe XIV	274.20, 264.79	6.2
Flare lines					
Fe XVIII	974.84	6.9	Ca XVII	192.82	6.7
Fe XX	721.55	7.0	Fe XXIII	263.76	7.2
			Fe XXIV	255.11	7.2

Table 5. SPICE emission lines, wavelength, temperature of formation, and the closest equivalents in IRIS.

SPICE	Wavelength (Å)	log T	IRIS	Wavelength (Å)	log T
H I	1025.72	4.0	Mg II	803, 2796	3.7–3.9
C II	1036.34	4.3	C II	1334, 1335	4.3
O IV	787.72	5.2	O IV	1399, 1401	5.2
Mg XI	997.44	6.2	Fe XII	1349.4	6.2
Flare lines					
Fe XX	721.55	7.0	Fe XXI	1354.1	7.0

to the low corona using three imaging telescopes: the Full Sun Imager (FSI) and two high-resolution imagers (HRI_{EUUV} and HRI_{Ly α}). The FSI provides a $3.8^\circ \times 3.8^\circ$ FOV in the 174 Å and 304 Å passbands with a typical temporal cadence of 600 s and a spatial resolution of 9 arcsec. This telescope provides a context view of the upper solar atmosphere up to $4 R_\odot$ at perihelion.

Both HRI_{EUUV} and HRI_{Ly α} telescopes provide a 17 arcmin \times 17 arcmin FOV with a plate-scale of 0.5 arcsec and unprecedented imaging cadence of 1 s. The passband of HRI_{EUUV} (174 Å) is comparable to that of FSI. The second high-resolution telescope, HRI_{Ly α} , observes the Sun in the Lyman α line (Ly α 1216 Å). The HRI instruments will study the small-scale structures and highly dynamic events in the upper solar atmosphere. Ly α is the most intense emission line in the solar spectrum and affects planetary atmospheres, so it is of great interest; however, to date observations in Ly α are rare and were carried out mainly aboard sounding rockets (Korendyke et al. 2001; Vourlidis et al. 2010, 2016; Chua et al. 2013; Chintzoglou et al. 2018) and the Transition Region and Coronal Explorer space observatory (Golub et al. 1999). Table 6 shows the closest corresponding SPICE emission line to the EUV passband. Again, caution must be used for the temperature of formation with Ly α , as it is a complex, optically thick spectral line.

6.3. Spacecraft separation angle and spatial resolution

6.3.1. 3D point triangulation uncertainties

An issue of great importance when planning observations with two spacecraft is understanding the optimum separation between them. In this section we discuss how the accuracy of the measurement varies with spacecraft separation. Inhester (2006)

Table 6. SPICE emission lines, wavelength, and temperature of formation, and the closest equivalent filter in EUV.

SPICE	Wavelength (Å)	log T	EUI	Wavelength (Å)	log T
C III	977.03	4.5	Ly α	1216	4.7
Mg VIII	772.31	5.9	Fe IX	174	5.9
Ne VIII	772.31	5.9	Fe IX	174	5.9

calculated that the errors in 3D coronal point triangulation depend on both the spatial resolution ds of an image and on the spacecraft separation angle γ :

$$\varepsilon_\Delta = \frac{ds}{\sin(\gamma/2)}. \quad (2)$$

Here ds is the pointing error across the epipolar line, which is linearly dependent on the spatial resolution of the instrument and can have values from 1 to 10 pixels, depending on the accuracy with which the same feature in two images can be identified. When the spatial resolution is fixed and $\gamma = 0$, the errors are very large. For large γ the errors are small, but additional errors are introduced due to complications in identifying the same feature in both images. When $\gamma = 180^\circ$, the errors are very large for off-limb features because the LOSs of the two spacecraft are parallel. The low optical thickness of the solar corona enables the observation of the same off-limb feature when the separation is near 180° , but makes it impossible to observe the same on-disc feature (Aschwanden et al. 2012b, 2015).

6.3.2. 3D coronal Loop triangulation uncertainties

The geometric error in Eq. (2) is the error for the triangulation of a single-point object. For a 1D object such as a section of a loop, the error is more complex, as it additionally increases with decreasing angle between the loop tangent and the epipolar plane, and theoretically becomes infinite if this angle becomes zero. The intuitive reason for this behaviour is that a smaller angle with the epipolar plane results in a smaller visual angle between the projected tangent and the epipolar lines in both images. Consequently, the point of intersection of the loop with the epipolar lines can be less well determined (Inhester 2006).

Aschwanden et al. (2012b) showed that stereoscopy of coronal loops is feasible with good accuracy from around 6° to 127° . This range is also predicted theoretically by taking into account the triangulation errors due to finite spatial resolution and uncertainty in the identification of stereoscopic correspondence in image pairs, which is disturbed by projection effects and foreshortening for viewing angles near the limb. By combining the accuracy of altitude triangulation with the stereoscopic correspondence ambiguity, the authors estimated that a spacecraft separation angle of 22° – 125° is most favourable for stereoscopy, when using an instrument with a spatial resolution of 2.6 arcsec (pixel size of 1.6 arcsec) such as EUV aboard STEREO.

We used Eq. (2) to calculate the triangulation errors for different spacecraft separation angles γ between the Solar Orbiter and the near-Earth spacecraft Hinode or IRIS. Figure 13 shows the triangulation error as a function of spacecraft separation angle, where ds is 1 pixel. The physical measure contained in a one-pixel unit will vary as (100–350) km² for HRI and as (900–3000) km² for FSI when the Solar Orbiter travels between apohelion and perihelion. The angle interval of 10° – 100° is expected

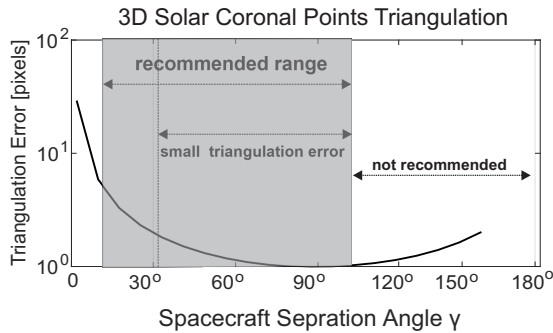


Fig. 13. Geometric error for triangulating a single-point object as a function of spacecraft separation angle. The object is observed by two separated spacecraft: the Solar Orbiter and one Earth-orbiting spacecraft (SDO, Hinode, or IRIS). The separation angles between the Earth-Sun line and the Solar Orbiter–Sun line varies over the whole range of angles during the cruise and nominal phase of the mission. Angles of $\pm 90^\circ$ provide the minimal triangulation error of 1.4 pixels for the 3D geometry reconstruction using Solar Orbiter high-resolution imagers HRI_{EUV} and HRI_{Ly α} . Separation angles greater than 100° between the spacecraft can complicate pointing at the same area of the Sun with two spectrometers and is therefore not recommended. However, the angle interval of 10° – 100° provides a sufficiently small triangulation error and good pointing possibilities for spectrometers.

to provide a sufficiently small triangulation error and good pointing possibilities for 3D solar spectroscopy.

7. Discussion and conclusions

We have developed a technique that reconstructs velocity vectors in coronal loops from the Doppler maps and EUV images obtained by two spacecraft located at significant distances from each other (on a heliospheric scale). The methodology is built upon the dynamic solar rotation EUV spectroscopy and on STEREO triangulation methods for coronal loops observed in optically thin coronal EUV emissions lines (Aschwanden 2011). Novel algorithms use methods of spatial analytical geometry in order to determine 3D velocities in coronal loops using different LOSs Doppler shifts measurements. The study is inspired by the launch of the Solar Orbiter in February 2020, the first solar mission to travel far beyond the ecliptic plane, which carries the EUV spectrometer. For the first time, stereoscopic pairs of solar Doppler maps will be available by combining data from the distant Solar Orbiter and the near-Earth spectrometers. We, therefore, explore the optimum conditions for future vector velocity observations with Solar Orbiter. The methodology consists of the following steps:

1. Determination of 3D geometry of structures through the LOS projection technique with high-resolution broad-band EUV imagers aboard the Solar Orbiter, the Solar Dynamics Observatory, and STEREO.
2. Cross-calibration and alignment between monochromatic and broad-band EUV images.
3. Vector velocity reconstruction
 - (a) Data acquisition: Stereoscopic pair of Doppler shifts at each coronal point.
 - (b) Deprojection 1D \rightarrow 2D: v_{LOS1} , $v_{\text{LOS2}} \rightarrow v_{\text{ep}}$. Two measured LOS velocity components are deprojected into velocity vector v_{ep} defined in the plane formed by the two spacecrafts and the coronal point we reconstruct the velocity vector. When orthogonally projected on LOS1

and LOS2, v_{ep} represents v_{LOS1} and v_{LOS2} velocities measured by each spectrometer.

- (c) Deprojection 2D \rightarrow 3D: $v_{\text{ep}} \rightarrow V_{3\text{D}}$. The velocity vector $V_{3\text{D}}$ is reconstructed by the orthogonal deprojection of the defined in the observational plane v_{ep} onto the direction of plasma flow in the 3D solar corona.
 - (d) Limits of application: If the plasma flow in the solar corona is orthogonal to the observational plane the velocity vector cannot be estimated.
4. Spacecraft separation set-up: The 3D solar spectroscopy methodology developed here can be applied efficiently over a wide range 10° – 100° of separation angles between Solar Orbiter SPICE and Hinode/EIS or IRIS for practically the entire duration of the Solar Orbiter mission, subject to observation of the same area in the Sun. The most favourable for spacecraft separation is expected to be 90° .

The first attempt of Doppler maps stereoscopic observations in coronal lines was conducted by the consortium during the Solar Orbiter cruise phase on 21–28 April 2021 as part of a quadrature observation campaign. Test data for vector velocity reconstruction will be available for the community shortly after calibration. Velocity vectors in plasma flows propagating at small angles to the observation plane (the epipolar plane, where the LOS Doppler velocities are located) can be reconstructed with higher accuracy, but the triangulation error may increase. The high spectral and spatial resolution of the instruments also contributes to an increase in the accuracy of the 3D velocity reconstruction (i.e. Solar Orbiter observations in perihelion positions minimise triangulation errors). The applicability of the methodology is determined by the correct solution of two problems, stereoscopic tie-pointing and triangulation of features, and application of analytical geometry in space. All these factors must be taken into account when planning stereoscopic observations using Solar Orbiter, and the detailed error assessment will be provided upon the algorithm test with real stereoscopic Doppler map datasets.

Acknowledgements. The authors acknowledge the anonymous referee for providing valuable suggestions and comments. We acknowledge ESA Solar Orbiter SOC, especially David Williams and Anik de Groof, also Miho Janvier for the stereoscopic observations planning with Solar Orbiter. We are grateful to the EU, SPICE instrument teams and to ESA Solar Orbiter Remote Sensing working group for detailed discussions during the consortium meetings, to Hardi Peter and Bart de Pontieu for discussions about the wavelengths and stereoscopic observations of Doppler maps. OP is grateful to Conrad Schwanitz for sharing his data analysis experience, William Thompson for the vector velocity definition velocity. OP acknowledges funding from Karbacher Fonds. KB acknowledges funding from SNSF. CM acknowledges grants PICT 2016-0221 (ANPCyT) and UBACyT 20020170100611BA. CM is a member of the Carrera del Investigador Científico of the Consejo Nacional de Investigaciones Científicas y Técnicas (CONICET). The authors thank the Belgian Federal Science Policy Office (BELSPO) for the provision of financial support in the framework of the PRODEX Programme of the European Space Agency (ESA) under contract numbers PEA 4000112292 and 4000117262.

References

- Anderson, M., Appourchaux, T., Auchère, F., et al. 2020, *A&A*, **642**, A14
 Aschwanden, M. J. 2009a, *Ann. Geophys.*, **27**, 3275
 Aschwanden, M. J. 2009b, *Space Sci. Rev.*, **149**, 31
 Aschwanden, M. J. 2011, *Liv. Rev. Sol. Phys.*, **8**, 5
 Aschwanden, M. J., & Bastian, T. S. 1994, *ApJ*, **426**, 425
 Aschwanden, M. J., & Wülser, J.-P. 2011, *J. Atm. Sol.-Terr. Phys.*, **73**, 1082
 Aschwanden, M. J., Lim, J., Gary, D. E., & Klimchuk, J. A. 1995, *ApJ*, **454**, 512
 Aschwanden, M. J., Newmark, J. S., Delaboudinière, J.-P., et al. 1999, *ApJ*, **515**, 842
 Aschwanden, M. J., Nitta, N. V., Wuelser, J.-P., & Lemen, J. R. 2008, *ApJ*, **680**, 1477

- Aschwanden, M. J., Wuelser, J.-P., Nitta, N. V., et al. 2012a, *ApJ*, **756**, 124
- Aschwanden, M. J., Wülser, J.-P., Nitta, N., & Lemen, J. 2012b, *Sol. Phys.*, **281**, 101
- Aschwanden, M. J., Schrijver, C. J., & Malanushenko, A. 2015, *Sol. Phys.*, **290**, 2765
- Baker, D., van Driel-Gesztelyi, L., Mandrini, C. H., Démoulin, P., & Murray, M. J. 2009, *ApJ*, **705**, 926
- Baker, D., Janvier, M., Démoulin, P., & Mandrini, C. H. 2017, *Sol. Phys.*, **292**, 46
- Barczynski, K., Peter, H., Chitta, L. P., & Solanki, S. K. 2018, *A&A*, **619**, A5
- Berton, R., & Sakurai, T. 1985, *Sol. Phys.*, **96**, 93
- Boutry, C., Buchlin, E., Vial, J. C., & Régnier, S. 2012, *ApJ*, **752**, 13
- Brooks, D. H., & Warren, H. P. 2011, *ApJ*, **727**, L13
- Chifu, I., Inhester, B., & Wiegmann, T. 2015, *A&A*, **577**, A123
- Chifu, I., Wiegmann, T., & Inhester, B. 2017, *ApJ*, **837**, 10
- Chintzoglou, G., De Pontieu, B., Martínez-Sykora, J., et al. 2018, *ApJ*, **857**, 73
- Chua, D. H., Korendyke, C., Vourlidas, A., Moses, J., & Brown, C. 2013, *AGU Fall Meet. Abstr.*, **2013**, SH13A
- Culhane, J. L., Harra, L. K., James, A. M., et al. 2007, *Sol. Phys.*, **243**, 19
- de Patoul, J., Inhester, B., Feng, L., & Wiegmann, T. 2013, *Sol. Phys.*, **283**, 207
- De Pontieu, B., McIntosh, S. W., Carlsson, M., et al. 2007, *Science*, **318**, 1574
- De Pontieu, B., Title, A. M., Lemen, J. R., et al. 2014a, *Sol. Phys.*, **289**, 2733
- De Pontieu, B., Rouppe van der Voort, L., McIntosh, S. W., et al. 2014b, *Science*, **346**, 1255732
- De Rosa, M. L., Schrijver, C. J., Barnes, G., et al. 2009, *ApJ*, **696**, 1780
- Del Zanna, G., & Mason, H. E. 2018, *Liv. Rev. Sol. Phys.*, **15**, 5
- Delannée, C., Artzner, G., Schmieder, B., & Parenti, S. 2014, *Sol. Phys.*, **289**, 2565
- Démoulin, P., Bagala, L. G., Mandrini, C. H., Henoux, J. C., & Rovira, M. G. 1997, *A&A*, **325**, 305
- Démoulin, P., Baker, D., Mandrini, C. H., & van Driel-Gesztelyi, L. 2013, *Sol. Phys.*, **283**, 341
- Dolla, L. R., & Zhukov, A. N. 2011, *ApJ*, **730**, 113
- Edwards, S. J., Parnell, C. E., Harra, L. K., Culhane, J. L., & Brooks, D. H. 2016, *Sol. Phys.*, **291**, 117
- Eyles, C. J., Harrison, R. A., Davis, C. J., et al. 2009, *Sol. Phys.*, **254**, 387
- Feng, L., Wiegmann, T., Inhester, B., et al. 2007a, *Sol. Phys.*, **241**, 235
- Feng, L., Inhester, B., Solanki, S. K., et al. 2007b, *ApJ*, **671**, L205
- Feng, L., Inhester, B., Solanki, S. K., et al. 2009, *ApJ*, **700**, 292
- Golub, L., Bookbinder, J., Deluca, E., et al. 1999, *Phys. Plasmas*, **6**, 2205
- Green, L. M., López fuentes, M. C., Mandrini, C. H., et al. 2002, *Sol. Phys.*, **208**, 43
- Harra, L. K., Sakao, T., Mandrini, C. H., et al. 2008, *ApJ*, **676**, L147
- Howard, T. A., & Tappin, S. J. 2008, *Sol. Phys.*, **252**, 373
- Howard, R. A., Moses, J. D., Vourlidas, A., et al. 2008, *Space Sci. Rev.*, **136**, 67
- Inhester, B. 2006, ArXiv e-prints [arXiv:astro-ph/0612649]
- Kaiser, M. L., Kucera, T. A., Davila, J. M., et al. 2008, *Space Sci. Rev.*, **136**, 5
- Klimchuk, J. A., Lemen, J. R., Feldman, U., Tsuneta, S., & Uchida, Y. 1992, *PASJ*, **44**, L181
- Korendyke, C. M., Vourlidas, A., Cook, J. W., et al. 2001, *Sol. Phys.*, **200**, 63
- Kosugi, T., Matsuzaki, K., Sakao, T., et al. 2007, *Sol. Phys.*, **243**, 3
- Koutchmy, S., & Molodenskii, M. M. 1992, *Nature*, **360**, 717
- Liewer, P. C., de Jong, E. M., Hall, J. R., et al. 2009, *Sol. Phys.*, **256**, 57
- Mandrini, C. H., Démoulin, P., van Driel-Gesztelyi, L., et al. 1996, *Sol. Phys.*, **168**, 115
- Mandrini, C. H., Nuevo, F. A., Vásquez, A. M., et al. 2014, *Sol. Phys.*, **289**, 4151
- Mandrini, C. H., Baker, D., Démoulin, P., et al. 2015, *ApJ*, **809**, 73
- Mierla, M., Davila, J., Thompson, W., et al. 2008, *Sol. Phys.*, **252**, 385
- Mierla, M., Inhester, B., Marqué, C., et al. 2009, *Sol. Phys.*, **259**, 123
- Mierla, M., Inhester, B., Antunes, A., et al. 2010, *Ann. Geophys.*, **28**, 203
- Müller, D., St. Cyr, O. C., Zouganelis, I., et al. 2020, *A&A*, **642**, A1
- Nisticò, G., Verwichte, E., & Nakariakov, V. 2013, *Entropy*, **15**, 4520
- Patsourakos, S., Vourlidas, A., Wang, Y. M., Stenborg, G., & Thernisien, A. 2009, *Sol. Phys.*, **259**, 49
- Pesnell, W. D., Thompson, B. J., & Chamberlin, P. C. 2012, *Sol. Phys.*, **275**, 3
- Phillips, G. J. H., Feldman, U., & Landi, E. 2008, *Ultraviolet and X-ray Spectroscopy of the Solar Atmosphere* (Cambridge: Cambridge University Press)
- Pizzo, V. J., & Biesecker, D. A. 2004, *Geophys. Res. Lett.*, **31**, L21802
- Podladchikova, T., Veronig, A. M., Dissauer, K., Temmer, M., & Podladchikova, O. 2019, *ApJ*, **877**, 68
- Reale, F. 2010, *Liv. Rev. Sol. Phys.*, **7**, 5
- Rochus, P. L., Auchere, F., Berghmans, D., et al. 2019, *AGU Fall Meet. Abstr.*, **2019**, SH21D
- Rodriguez, L., Zhukov, A. N., Gissot, S., & Mierla, M. 2009, *Sol. Phys.*, **256**, 41
- Sandman, A. W., Aschwanden, M. J., Derosa, M. L., Wülser, J. P., & Alexander, D. 2009, *Sol. Phys.*, **259**, 1
- Stenborg, G., Vourlidas, A., & Howard, R. A. 2008, *ApJ*, **674**, 1201
- Temmer, M., Preiss, S., & Veronig, A. M. 2009, *Sol. Phys.*, **256**, 183
- Thompson, W. T. 2006, *A&A*, **449**, 791
- Vourlidas, A., Sanchez Andrade-Nuño, B., Landi, E., et al. 2010, *Sol. Phys.*, **261**, 53
- Vourlidas, A., Beltran, S. T., Chintzoglou, G., et al. 2016, *J. Astron. Instrum.*, **5**, 1640003
- West, M. J., Zhukov, A. N., Dolla, L., & Rodriguez, L. 2011, *ApJ*, **730**, 122
- Wiegmann, T., & Neukirch, T. 2002, *Sol. Phys.*, **208**, 233
- Wiegmann, T., Inhester, B., & Feng, L. 2009, *Ann. Geophys.*, **27**, 2925
- Wuelser, J. P., Lemen, J. R., Tarbell, T. D., et al. 2004, in *SPIE Conf. Ser.*, eds. S. Fineschi, & M. A. Gummin, 5171, 111